Modeling the effect of free convection on permafrost melting-rates in frozen rock-clefts

Amir Sedaghatkish[1,2], Frédéric Doumenc[3,4], Pierre-Yves Jeannin[1], Marc Luetscher[1]

[1]Swiss Institute for Speleology and Karst Studies (SISKA), CH-2300, La Chaux-de-Fonds, Switzerland
[2]Center for Hydrogeology and Geothermics (CHYN), University of Neuchâtel, 2000 Neuchâtel, Switzerland
[3]Univèrsité Paris-Saclay, CNRS, FAST, 91405, Orsay, Rue André Rivière, France
[4]Sorbonne Université, UFR 919, 4 place Jussieu, F-75252, Paris Cedex 05, France

Correspondence to: Amir Sedaghatkish (amir.sedaghatkish@isska.ch)

Abstract. This research develops a conceptual model of a karst system subject to mountain permafrost. The transient thermal response of a frozen rock-cleft after the rise of the atmosphere temperature above the melting temperature of water is investigated by numerical simulations. Free convection in liquid water (i.e., buoyancy-driven flow) is considered. The density increase of water from 0 to 4°C causes warmer meltwater to flow downwards and colder upwards, resulting in significant enhancement of the heat transferred from the ground surface to the melting front. Free convection increases the melting rate by approximately an order of magnitude compared to a model based on thermal conduction in stagnant water. The model outcomes are compared qualitatively with field data from Monlesi ice cave (Switzerland) and confirm the agreement between real-world observations and the proposed model when free convection is considered.

Keywords: Numerical modeling, free convection, melting rate, conduction, permafrost, karst, cave, hydrogeology

1 Introduction

With global climate change and rising temperatures, permafrost degradation has become a significant concern (Duvillard et al., 2021; Walvoord and Kurylyk, 2016; Jin et al., 2021). This is particularly true in mountain regions where rapid thawing causes subsidence and rockfalls impacting construction works and tourist facilities (Haeberli et al., 2017). Thawing permafrost poses serious challenges to infrastructures built on frozen ground, including buildings, roads, pipelines, and railways (Larsen et al., 2008; Cheng, 2005; Pham et al., 2008; Zhang et al., 2005; Fortier et al., 2011). Permafrost acts as a natural barrier, preventing water from infiltrating into the ground. As it thaws, drainage patterns are altered, leading to increased erosion and discharge of groundwater to rivers and lakes (Bense et al., 2012; Andresen et al., 2020; Fabre et al., 2017; Painter et al., 2016;

30   Walvoord and Kurylyk, 2016). Permafrost degradation can also disrupt ecosystems adapted to frozen conditions. Trees, plants, and wildlife that rely on permafrost stability may struggle to adapt to climate changes, leading to shifts in species distribution and ecosystem dynamics depending on the permafrost melting rate (Hayward et al., 2018; Krumhansl et al., 2015; Pelletier et al., 2018).

Field measurements in boreholes (e.g. Noetzli et al., 2021; Haberkorn et al., 2021) and caves (Luetscher et al., 2008; Colucci
35   and Guglielmin, 2019; Wind et al., 2022) have shown that heat advected by water and air fluxes may significantly disturb the geothermal field, challenging classical models of heat propagation based on conductive fluxes. In carbonate environments, in particular, the infiltration of water along well-developed conduits may develop a thermal anomaly deep into the karst system. The discontinuous nature of permafrost in karst environments may lead to the formation of massive cave ice at depth (Bartolomé et al., 2022) but also explain unexpected speleothem formations during glacial times (Luetscher et al., 2015;
40   Fohlmeister et al., 2023; Fohlmeister et al., 2023).

Efforts are being made to study and understand permafrost degradation to mitigate its impacts. So far, most studies considered mainly conductive and latent heat fluxes (Malakhova, 2022; Galushkin, 1997; Ivanov and Rozhin, 2022; Marchenko et al., 2008; Schuster et al., 2018; Jafarov et al., 2012; Cicoira et al., 2019; Hornum et al., 2020). Such models are, however, not applicable to heterogeneous, ice-rich media including debris-slopes, rock glaciers, fractured and/or karst aquifers. But, even
45   though conventional 1D transient models are not suitable to every context, they offer several advantages including lower computational costs than 2 or 3D models and easy implementation. Pruessner et al., (2021) investigated glacier runoff associated with permafrost degradation in high Alpine catchments. They used two different methods GERM (Huss et al., 2008) and SNOWPACK (Bartelt and Lehning, 2002) which are based on 1D transient conduction considering latent heat exchanges, different thermal properties of ground layers constituents and ventilation effects. This distributed model is efficient for
50   calculation of temperature in large domains (catchment scale). Mohammed et al., (2021) developed a hydro-thermal-solutal model for analyzing reactive solute transport in permafrost-affected groundwater system by considering convective flux in the energy balance. Tubini et al., (2021) proposed a numerical approach for modeling heat transfer of permafrost thawing based on conduction and latent heat flux in 1D domain which is capable to deal with high time steps and maintains conservation of energy in long-term simulations. Hasler et al., (2011) built a conceptual model combining numerical modeling and laboratory
55   experiments to investigate the effect of advective heat transport induced by water drainage in frozen rock clefts and fractures at small scales. They built a conceptual model combining numerical modelling and laboratory experiments. These authors find a significant effect of water flow inside the clefts, due to the formation of thermal shortcuts between the atmosphere and the subsurface.

Although, the majority of these studies are designed to address large-scale problems they typically neglect free convection
60   within the liquid water phase. This process could nonetheless play an important role in the total heat transfer particularly in geographically restricted areas subject to mountain permafrost (Haberkorn et al., 2021). Figure 1-a displays the bottom of a frozen cleft hosted in an Alpine karst. Such clefts and fissures are characterized by distinct geometries accommodating contrasted volumes of ice. Our aim is to study the effect of free convection on the melting rate in frozen rock clefts and/or

karst conduits at daily scale. Atmospheric warming at the upper boundary melts the ice from top of the fractures, and increases

65 the meltwater temperature. While most fluids expand as temperature increases, liquid water shrinks when warmed from 0°C to 4°C. Above this temperature, the common behavior is recovered (see the maximum density at 4°C in Fig.2). Therefore, the progressive warming of the meltwater at the top of the cleft results in an unstable situation (heavier fluid above lighter) that triggers free convection (buoyancy-driven flow). To assess the thermal reaction time, and thus hydrological breakthrough associated with the thawing of mountain permafrost we model the heat exchange in a frozen rock cleft. We assess by numerical

70 simulations the temperature field in the meltwater, ice, and surrounding rock, as well as the velocity field within the liquid water to elucidate the main mechanisms driving the thawing of ice. Although a physical monitoring of such processes is hardly possible, our model fits as close as possible to effective field observations. A systematic comparison is conducted under similar thermal settings for two cases: one considers heat conduction in stagnant liquid water (SLW) whereas free convection (FC) is taken into account in the second case. Our study shows how free convection enhances the melting rate of an ice cleft at different

75 aperture sizes.

2 Computational domain and governing equations

2.1 Physical model and simplifying assumptions

We consider the upper part of a single vertical cleft of size aperture A_p filled with pure water whose melting point is $T_m = 0°C$. This cleft is surrounded by a rock mass of width W (see Fig.1-b). In karst massifs, water flow concentrates in well-defined

80 conduits (Ford and Williams, 2007). The micro-porosity of the rock is thus disregarded, and impermeable rock mass is assumed.

The cleft is located at the center of the 2D domain of height H_{dom}. In the initial state, the system (water and surrounding rock) is at the uniform initial temperature T_i=-1°C, and all the water is frozen. At time t=0, the temperature of the ground surface T_s increases at the constant rate 1.77 °C/hour to reach 15°C after 9 hours. This temperature increase is similar to the daily warming

85 between the early morning and the afternoon.

The effect of the cleft aperture size was investigated by varying A_p from 2 cm to 50 cm. We imposed H_{dom}=0.8 m and W=1 m in all simulations. These values are large enough so that the thermal perturbation induced by the presence of the cleft does not reach the domain boundaries at the end of the simulated time (9 hours). The vertical and bottom boundaries of the domain can therefore be considered as adiabatic (see Fig.1-b). It is important to note that the domain height H_{dom} contains only the upper

90 part of the cleft, whose actual depth commonly ranges from 1 to 10 m. The value of H_{dom} used in this study is convenient for the daily time scale considered in the numerical simulations. Simulating larger time scales would require larger values of H_{dom}.

2.2 Governing equations

The temperature T is the only dependent variable in the impermeable rock domain. It satisfies the standard heat equation

$$\rho_r c_{p,r} \frac{\partial T}{\partial t} = k_r \left(\frac{\partial^2 T}{\partial x^2} + \frac{\partial^2 T}{\partial z^2} \right) \tag{1}$$

95

where ρ_r, $c_{p,r}$ and k_r are the rock density, specific heat and thermal conductivity, respectively. z is the depth and x the horizontal distance from the symmetry plane of the cleft (see Fig. 1-b).

The water domain is more intricate. The velocity field must be calculated in the liquid part of the domain, but reduces to zero in the frozen region. To avoid the difficult task consisting in tracking the moving boundary between ice and liquid water, we

100 adopted a strategy that allows to define the same set of dependent variables and governing equations in the entire water domain. To this end, we do the approximation of smooth phase transition between solid and liquid phases. We assume that ice melting begins at temperature $T_{m1} = T_m - \Delta T$ and ends at $T_{m2} = T_m + \Delta T$ (water is in solid state for $T < T_{m1}$, in liquid state for $T < T_{m2}$, and both phases coexist for $T_{m1} \leq T \leq T_{m2}$). It is important to note that in this study, ΔT is a numerical parameter with no physical meaning. Ideally, the behavior of a pure substance melting at temperature T_m is recovered for $\Delta T \to 0$.

105 Decreasing ΔT thus improves the model accuracy, but requires more computational resources (see (Michałek and Kowalewski, 2003; Zeneli et al., 2019; Bourdillon et al., 2015; Arosemena, 2018) for more details). Practically, the setting of ΔT results from a sensitivity analysis. Its value must be decreased until it does not change the results. This is the purpose of appendix A, where it is shown that the model is a good approximation of a pure substance for $\Delta T \leq 0.7°C$.

The dependent variables defined in the water domain are the temperature T, the horizontal and vertical components of the

110 velocity vector u and v, the pressure p and the liquid volume fraction θ. Because of the assumption of smooth phase transition, θ varies continuously from 0 (solid phase) to 1 (liquid phase) throughout the water domain (see Fig.1-b). The corresponding governing equations read:

$$\frac{\partial u}{\partial x} + \frac{\partial v}{\partial z} = 0 \tag{2}$$

$$\rho_0 \frac{\partial u}{\partial t} + \rho_0 \left(u \frac{\partial u}{\partial x} + v \frac{\partial u}{\partial z} \right) = -\frac{\partial p}{\partial x} + \mu \left(\frac{\partial^2 u}{\partial x^2} + \frac{\partial^2 u}{\partial z^2} \right) + A \frac{(1-\theta)^2}{\theta^3 + \varepsilon} u \tag{3}$$

$$\rho_0 \frac{\partial v}{\partial t} + \rho_0 \left(u \frac{\partial v}{\partial x} + v \frac{\partial v}{\partial z} \right) = -\frac{\partial p}{\partial z} + \mu \left(\frac{\partial^2 v}{\partial x^2} + \frac{\partial^2 v}{\partial z^2} \right) - \rho_0 g \beta (T - T_0) + \rho_0 g + A \frac{(1-\theta)^2}{\theta^3 + \varepsilon} v \tag{4}$$

$$\rho c_p \frac{\partial T}{\partial t} + \rho c_p \left(u \frac{\partial T}{\partial x} + v \frac{\partial T}{\partial z} \right) - k \left(\frac{\partial^2 T}{\partial x^2} + \frac{\partial^2 T}{\partial z^2} \right) = 0 \tag{5}$$

$$\theta = \begin{cases} 0 & T < T_{m1} \quad \text{(Solid)} \\ \dfrac{T - T_{m1}}{T_{m2} - T_{m1}} & T_{m1} \le T \le T_{m2} \quad \text{(Diphasic)} \\ 1 & T > T_{m2} \quad \text{(Liquid)} \end{cases} \tag{6}$$

This set of equations includes the mass balance Eq.(2), the momentum balance Eqs.(3-4), the energy balance Eq.(5) and the relation between the liquid volume fraction θ and the temperature field Eq.(6). g is the gravity acceleration, ρ_0 is the density of liquid water at the reference temperature T_0, μ and β are the dynamic viscosity and thermal expansion coefficient of liquid water, ρ, c_p and k are the density, specific heat and thermal conductivity of water.

The last term in Eqs.(3-4) is used to impose the velocity transition between the liquid and solid phases. A and ε are numerical parameters imposed by the user. A must be as large as possible provided that solver stability is insured. In contrast, ε is a small parameter used to prevent divisions by zero in numerical calculations (Mousavi Ajarostaghi et al., 2019). It can be demonstrated that for $\theta = 0$ (i.e., in the solid phase), the solution of Eqs.(2-4) turns to $u \simeq v \simeq 0$, which is the solution expected in the solid phase (see Nazzi Ehms et al (2019) and Caggiano et al (2018) for more details). Conversely, the last term in Eqs.(3-4) vanishes for $\theta = 0$ (i.e., in the liquid phase). In this case, Eqs.(3-4) turns to the standard Navier-Stokes equations (momentum balance in an incompressible Newtonian fluid), required to calculate the velocity field in the liquid phase.

The boundary conditions are as follows. At the interface between an impermeable solid and a viscous fluid, the fluid velocity is equal to that of the solid (Guyon et al., 2015). This is the so-called no-slip and impermeability conditions, resulting in $u = v = 0$ at the rock-water interface. The temperature continuity and the heat flux conservation through this interface are also considered (since the water velocity vanishes at the rock-water interface, the heat flux through the interface reduces to conduction). As already mentioned in section 2.1, the bottom and vertical external boundaries are adiabatic, and the temperature evolution of the top boundary T_s increases at a constant rate (see Fig.1-b).

2.3 Material properties

The physical properties used in the simulations are listed in Table_1. Subscripts "r","s" and "l" refer to rock, ice and liquid water respectively. No subscript indicates the effective physical properties considered in the governing equations of the water domain (solid, liquid and diphasic). They are estimated from the liquid volume fraction θ as follows:

$$\rho = \rho_s (1-\theta) + \rho_l \theta \tag{7}$$

$$k = k_s (1-\theta) + k_l \theta \tag{8}$$

$$c_p = \frac{\rho_s c_{p,s} (1-\theta) + \rho_l c_{p,l} \theta}{\rho} + L_m \frac{\partial \alpha_m}{\partial T} \quad \text{with} \quad \alpha_m = \frac{1}{2} \frac{\rho_l \theta - \rho_s (1-\theta)}{\rho_l \theta + \rho_s (1-\theta)} \tag{9}$$

$$\mu = \mu_l \tag{10}$$

The effective specific heat c_p defined in Eq.(9) takes into account the latent heat of melting L_m.

The standard Boussinesq approximation is assumed in the liquid phase (Spiegel and Veronis, 1960; Bejan, 2013). This approximation, widely used for free convection modeling, consists in assuming constant liquid density in the governing equations Eqs.(2-4), except in the buoyancy term of the momentum balance equations Eqs.(3-4). The thermal expansion coefficient β at the origin of buoyancy is estimated from the relation

$$\beta = -\frac{1}{\rho_l}\frac{d\rho_l}{dT} \tag{11}$$

where ρ_l is the temperature-dependent liquid water density displayed in Fig.2 (the order of magnitude of β in the unstable temperature range from 0 to 4°C is approximately -3×10^{-5} K^{-1}). In contrast, the constant liquid density ρ_0 estimated at the reference temperature T_0 is considered in the inertia terms of Eqs.(3-4) ($\rho_0 = 999.84$ kg/m^3 at $T_0 = 0$°C). The Boussinesq approximation is valid if the maximum fluid density variation $\Delta\rho_l$ is much lower than the liquid density ρ_l, a condition usually satisfied in liquids ($\Delta\rho_l/\rho_l \sim 10^{-3}$ in our case).

The density of water is greater than that of ice by approximately 10%. This induces a reduction of volume upon melting which is neglected in our model. This is equivalent to assuming that an external water flow replenishes the top layer domain with water at the ground surface temperature T_s. This would result in the additional vertical velocity in the liquid phase (Heitz and Westwater, 1970):

$$v_l = \frac{(\rho_l - \rho_s)}{\rho_l}\frac{dH}{dt} \tag{12}$$

This velocity would be that of the liquid in the absence of free convection, or would be added to the free convection velocity field in the other case. This contraction-induced flow can be neglected if the heat advected in that way is negligible compared to the heat absorbed by the motion of the melting front:

$$\rho_l\, v_l\, c_{pl}(T_s - T_m) \ll L_m\rho_s\frac{dH}{dt} \tag{13}$$

Eqs.(12-13) yield the condition of validity:

$$\frac{(\rho_l - \rho_s)}{\rho_s}\frac{c_{pl}(T_s - T_m)}{L_m} \ll 1 \tag{14}$$

with the physical properties of table 1 and $T_s - T_m = 15$°C, the LHS of Eq.(14) is approximately equal to 0.02, much lower than 1. The volume change induced by melting can thus be safely neglected. Heitz and Westwater (1970) presented a comparison of mathematical solutions with equal and unequal phase densities. In a configuration close to ours, they show that considering equal densities for ice and liquid water resulted in a negligible loss of accuracy.

2.4 Numerical methods

The system of partial differential equations (Eqs. 1-6) was solved by finite elements using the software Comsol Multiphysics version 6.0 (Galerkin method with quadratic Lagrangian elements, time discretization by implicit backward differentiation formula).

The mesh density close to the walls was refined due to the high gradient of velocity and a structured (mapped) mesh type was
165 used for the water-ice domain as shown in Fig. 1-c. The mesh was validated by a sensitivity analysis comparing four different mesh qualities, with 14,000, 24,000, 32,000, and 47,000 elements, respectively. The difference in the results between the latter three cases was found to be insignificant. The mesh with 24,000 elements was thus selected in all simulations.

Regarding the numerical parameters required to model melting, we imposed ΔT=0.5 °C, A =1000 kg.m^{-3}.s^{-1} and $\varepsilon = 10^{-3}$.
170 We checked that imposing $\Delta T = 0.3$ °C or 0.7 °C did not significantly change the results (see Appendix A). The selected values of A and ε produced vanishingly small velocity fields in the ice with no deterioration of the solver stability.
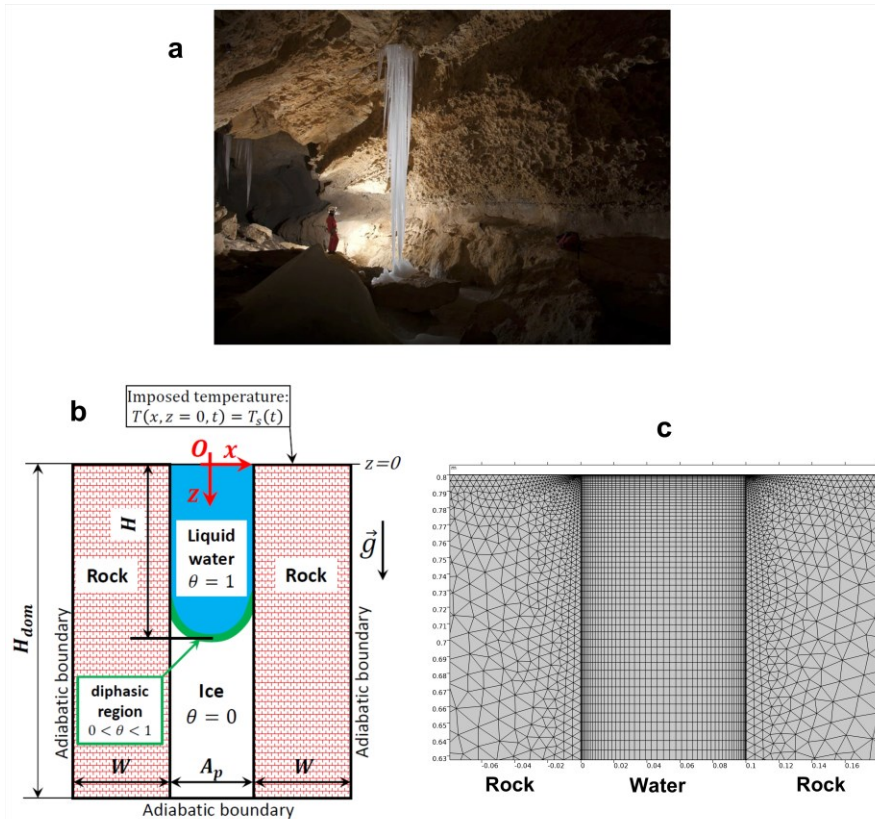
Figure 1. a) Pingouins cave, Switzerland, showing ice-filled clefts exposed on the cave roof (Photo courtesy A. Conne) b) Computational domain with external boundary conditions; 2 cm $\leq A_p \leq$ 50 cm, H_{dom}=0.8 m and W_{dom}=1 m (the sketch is not at scale) c) Finite element mesh in the upper part of the computational domain.

Table 1. Thermal properties and numerical parameters. The liquid water properties are temperature dependent. The properties of ice and rock are assumed constant.

Thermal properties	values	Reference
ρ_s (kg/m³)	916.2	-
k_s (W/m/K)	2.22	-
$c_{p,s}$ (J/kg/K)	2050	-
ρ_l (kg/m³)	see Fig.2	(Comsol Multiphysics)
k_l (W/m/K)	0.556 at 0°C 0.585 at 15°C	(Comsol Multiphysics)
$c_{p,l}$ (J/kg/K)	4216 at 0°C 4192 at 15°C	(Comsol Multiphysics)
μ_l (mPa.s)	1.79 at 0°C 1.43 at 7.5°C 1.15 at 15°C	(Comsol Multiphysics)
ρ_r (kg/m³)	2320	(Covington et al., 2011)
k_r (W/m/K)	1.656	(Guerrier et al., 2019)
$c_{p,r}$ (J/kg/K)	810	(Covington et al., 2011)
L_m (J/kg)	334000	(Weast, 1986)
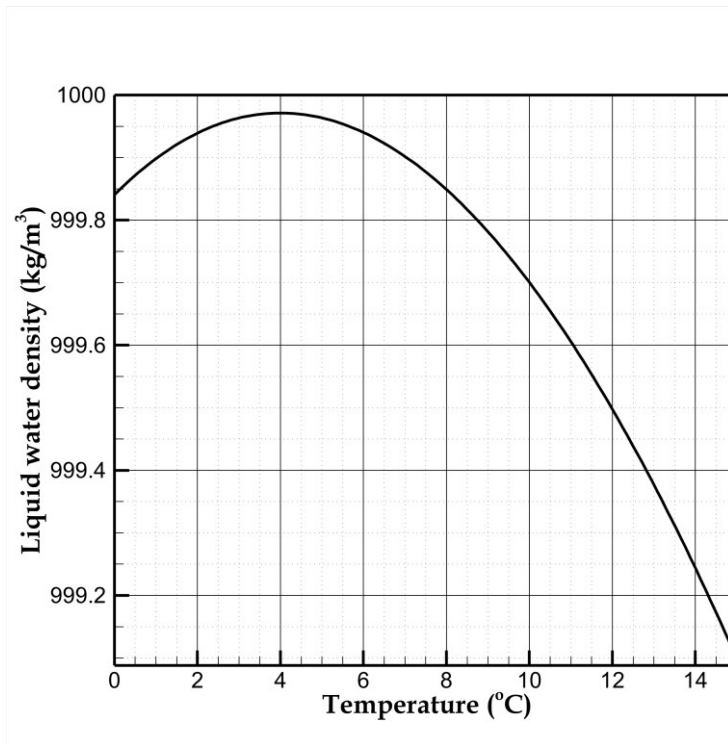
Figure 2. density of liquid water as a function of temperature (Comsol Multiphysics)

3 Model validation

The validity of our model is tested by comparison with two studies from the literature. A simple test case assuming stagnant liquid water (no free convection) was selected as a first step (numerical simulation of ice freezing by Kahraman et al., 1998). In a second step, our model was tested against experimental results including free convection (ice melting experiment by Virag et al., 2006).

3.1 Stagnant liquid water

When free convection is neglected, conduction and latent heat fluxes are the only mechanisms transferring heat in liquid water and ice. We compare our results with the results from (Kahraman et al., 1998). These authors developed a model to examine the heat transfer of ice melting inside a 20 cm×20 cm square assuming stagnant liquid water. A brief description of their conceptual model is given in Fig. 3-a. Ice is at an initial temperature of -30℃ and is exposed to a temperature of 20 °C over half of the lower boundary ($0 \le x \le 10$ cm, $y = 0$ cm) and 70℃ over the other half ($10 \le x \le 20$ cm , $y = 0$ cm). The temperature of the solid ice at the top boundary ($y = 20$ cm) is maintained at 0 °C and the other surfaces (left and right sides)

are insulated (Fig. 3-a). Figure 3-b shows the temperature distribution after 5 hours modelled in the present work. Temperature profiles at $x=4$ cm and $x=16$ cm in different times of melting can be seen in Fig. 3-c and d, respectively. The result of our model is in good agreement with (Kahraman et al., 1998).
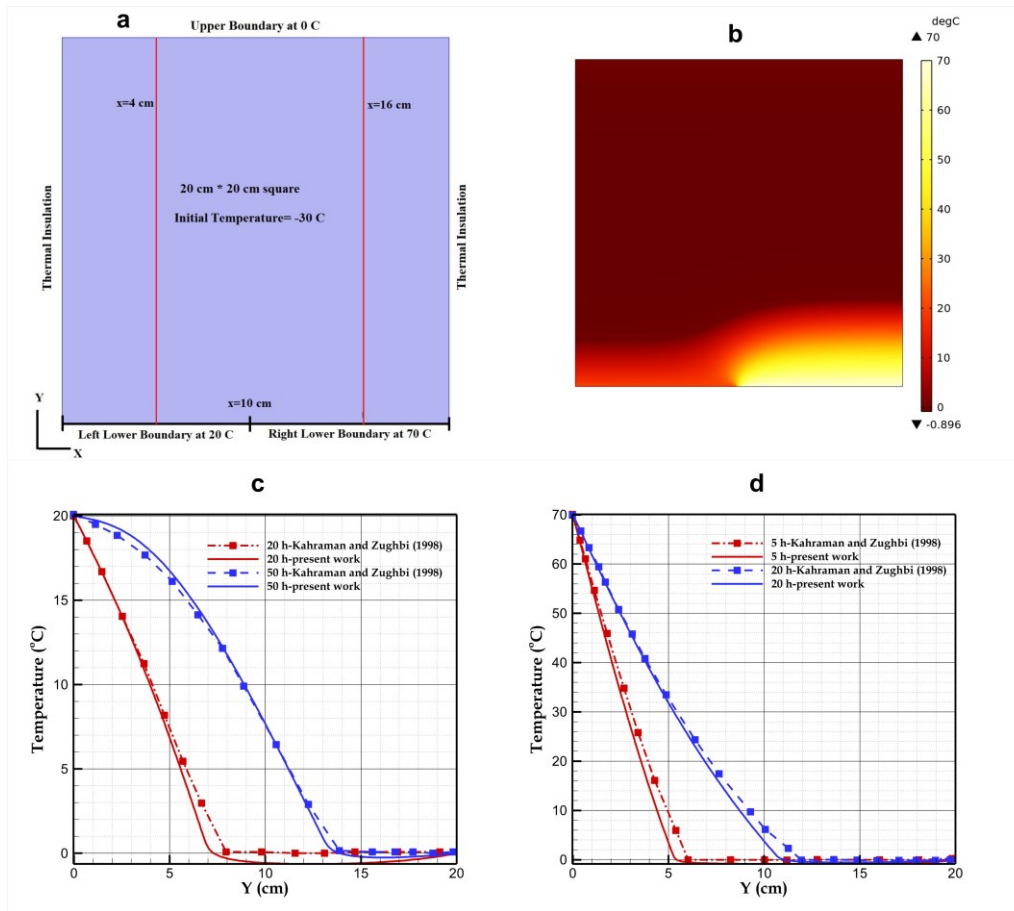
Figure 3. a) model geometry including initial and boundary conditions b) contour of temperature at t=5 hr c) temperature profile of ice and water at different times of ice melting at *x*=4 cm and d) *x*=16 cm

3.2 Free convection

Virag et al., (2006) investigated with an experimental approach the effect of free convection on ice melting inside a cavity shown in Fig. 4-a. The lower and top surfaces are thermally insulated. The left and right boundaries are at 0 and 8 °C, respectively. Figure 4-b displays contours of temperature (left) and the velocity field as well as velocity vectors (right) predicted by our model. The black arrows indicate the direction of the water flow. The model predicts the existence of two

contra-rotating free convection cells separated by the 4°C isotherm, which corresponds to the maximum liquid water density. In the small cell located in the lower left corner, where temperature is higher than 4°C, the liquid rises upward along the warm wall, as expected when the liquid density is a decreasing function of temperature. In the bigger cell located in the upper part of the liquid region, where the temperature is less than 4°C, the warmer liquid moves downward, as expected when the liquid density increases with temperature. Furthermore, results show that where the temperature gradient is high, the magnitude of the local velocity increases. This is seen next to the left boundary and also close to the ice interface. The convection-induced mixing homogenizes the temperature in the liquid phase.

Our numerical model replicates the melting front positions measured at different times by Virag et al. (2006) (see Fig. 5). Although some discrepancies exist between the experiments and the numerical model, especially at the bottom of the cavity at the beginning of the simulation and in the upper part at later times, the overall performance of our model is suitable to represent the free convection cells and their effect on ice melting despite the simplifying assumptions made in the model (2D geometry, negligible volume contraction upon melting, smooth solid-liquid transition).
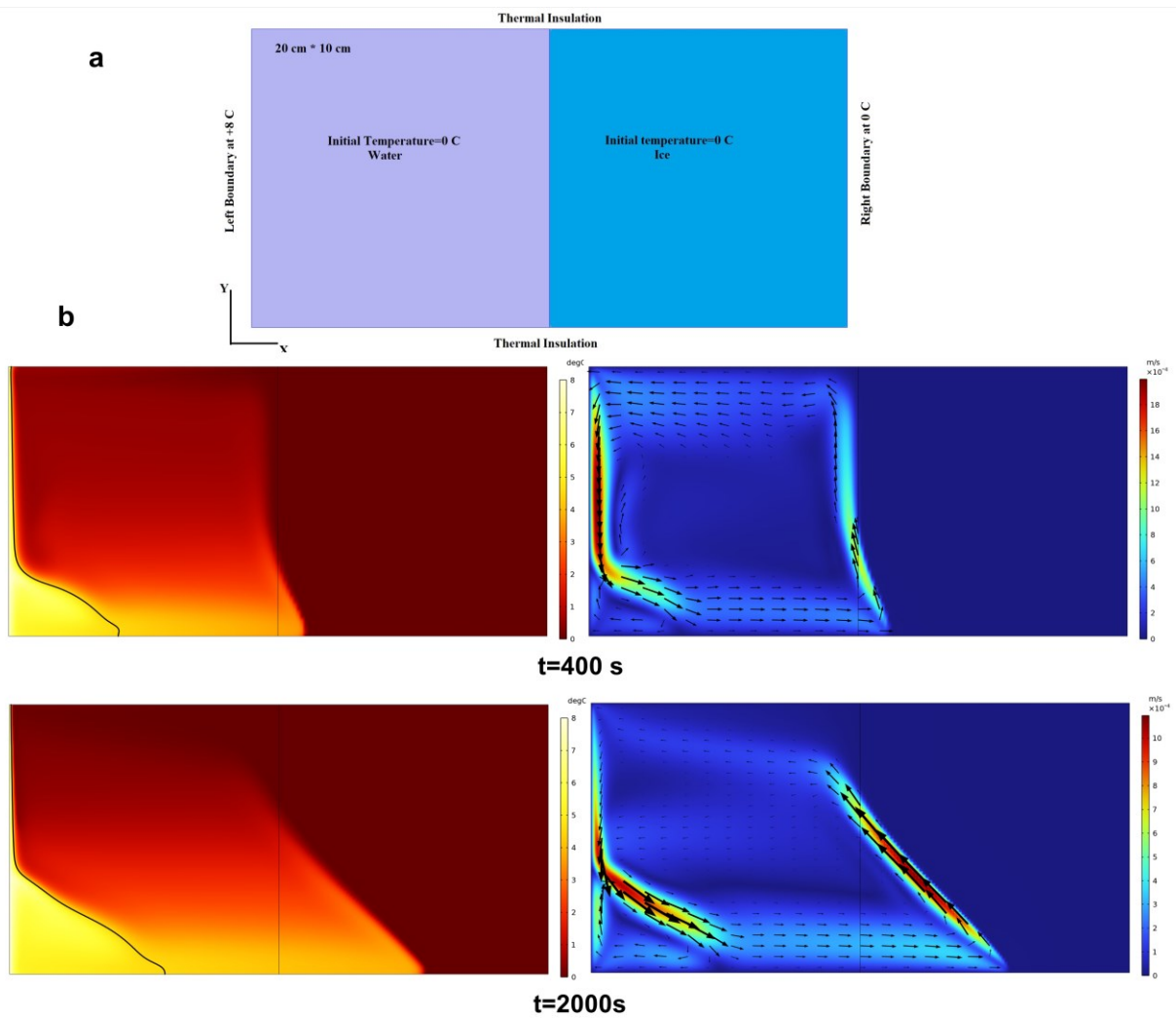
Figure 4. a) Computational domain including boundary and initial conditions in (Virag et al., 2006), b) results at times *t*=400 and 2000 s; left: temperature (the black line represents the isotherm *T*=4 °C); right: velocity magnitude.
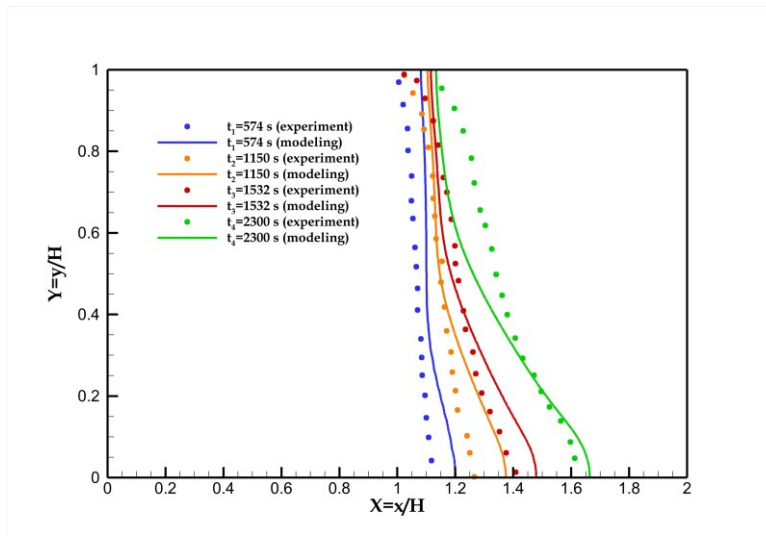
Figure 5. Evolution of the modeled ice-water interface during melting in comparison with experimental data by (Virag et al., 2006)

4 Results

4.1 Stagnant liquid water (SLW) versus free convection (FC)

The effect of free convection in heterogeneous, ice-filled karst environment (cf Fig. 1), where the medium is surrounded by rock and prone to atmospheric warming from the top surface was conceptualized in section-2. Here, we investigate the effect of free convection in more details considering two scenarios under identical thermal settings: 1) stagnant liquid water (SLW) and 2) free convection in liquid water (FC). Figure 6 illustrates the ice volume fraction $(1 - \theta)$ for different time steps at 3, 6 and 9 hours for these two scenarios, for an aperture size A_p=10 cm (see Fig. 1-b for a description of the computational domain geometry). For each specified time step, the SLW results are shown on the left and the FC results on the right. The difference between these two scenarios in terms of melting rate is obvious. When convection is disregarded (SLW), the melting front is nearly horizontal except close to the walls, where a steep slope is observed. The higher thermal diffusivity of the rock (

$\alpha_r = \dfrac{k_r}{\rho_r \, c_{p,r}} = 8.8 \times 10^{-7}$ m²/s) compared to that of the liquid water ($\alpha_l = \dfrac{k_l}{\rho_l \, c_{p,l}} = 1.3 \times 10^{-7}$ m²/s) results in faster heat

propagation in the rock, and enhanced melting of the ice closer to the rock. When free convection is considered (FC), the advection of heat by the flow results in faster propagation of the melting front, with an inversion of its curvature (the meting front propagates faster in the center of the cleft than close to the walls).
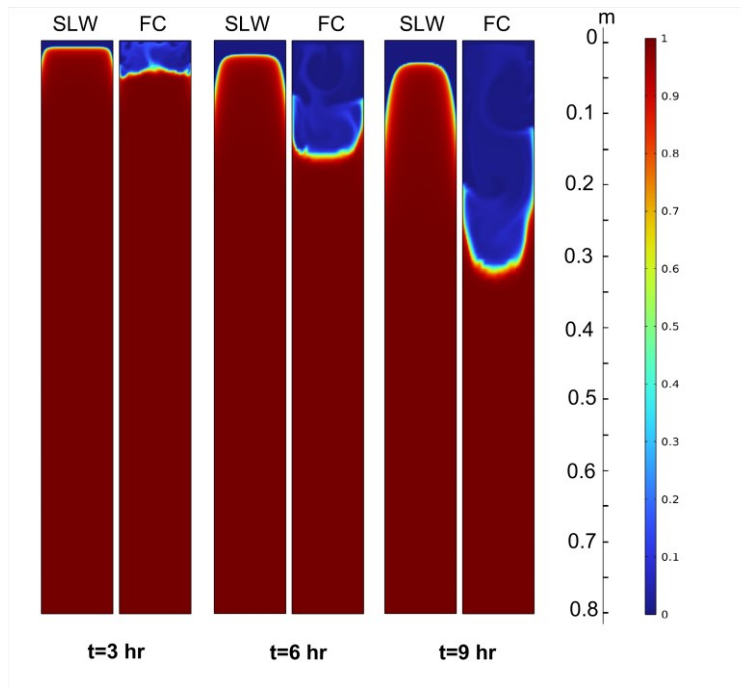
Figure 6. contour of the ice volume fraction $(1 - \theta)$ for stagnant liquid water (SLW) and free convection (FC). A_p=10 cm, H_{dom}=0.8 m and W=1 m .

Figure 7 displays the melting rate for both previous scenarios, SLW and FC. Because the initial temperature was -1 °C, the melting starts with c.1h delay, in both cases. Then the melting rate and the meltwater depth increase with time in response to the temperature increase at the top surface. After 9 hours, the melting rate is nearly an order of magnitude larger for FC (5.1 kg/s) than for SLW (0.6 kg/s). An animation file showing the evolution of the ice fraction can be found in the video supplement of the manuscript (Sedaghatkish and Luetscher, n.d.).

Figure 8 displays the temperature field of ice, water and surrounding rock after 9 hours. In FC case, most of the melted part of the cleft is in the temperature range from 0 to 1°C, with a high temperature gradient localized in a thin layer close to the ground surface (Fig. 8-b). In contrast, the temperature field in SLW case varies more evenly from the ground surface to the melting front (Fig. 8-a). This confirms that the circulation of water inside the cleft results in a thermal bridge between ice interface and top atmosphere. The extent of the mixing zone induced by FC can be much higher than the diffusion length in the case of SLW.

Figure-9 displays the left wall temperature as function of depth at different times for both scenarios. Although the melting rate for FC at t=3 hr is much higher than for SLW at the same time, their corresponding wall temperatures are close from each other. At larger times, the distinction between scenarios becomes more pronounced due to the increasing intensity of free convection.
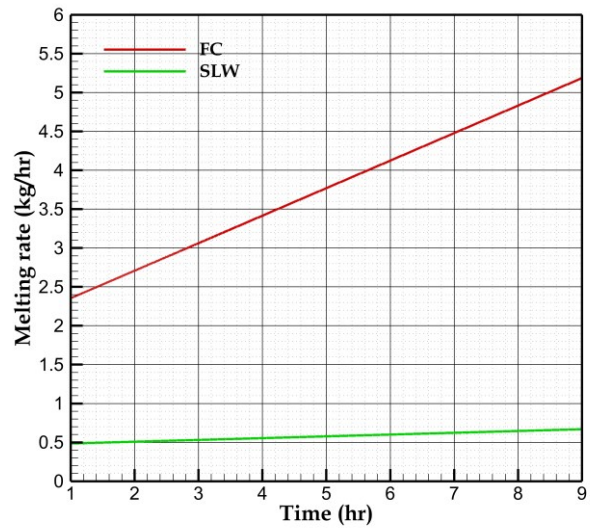
Figure 7. Melting rate versus time considering stagnant liquid water (SLW) and free convection (FC).
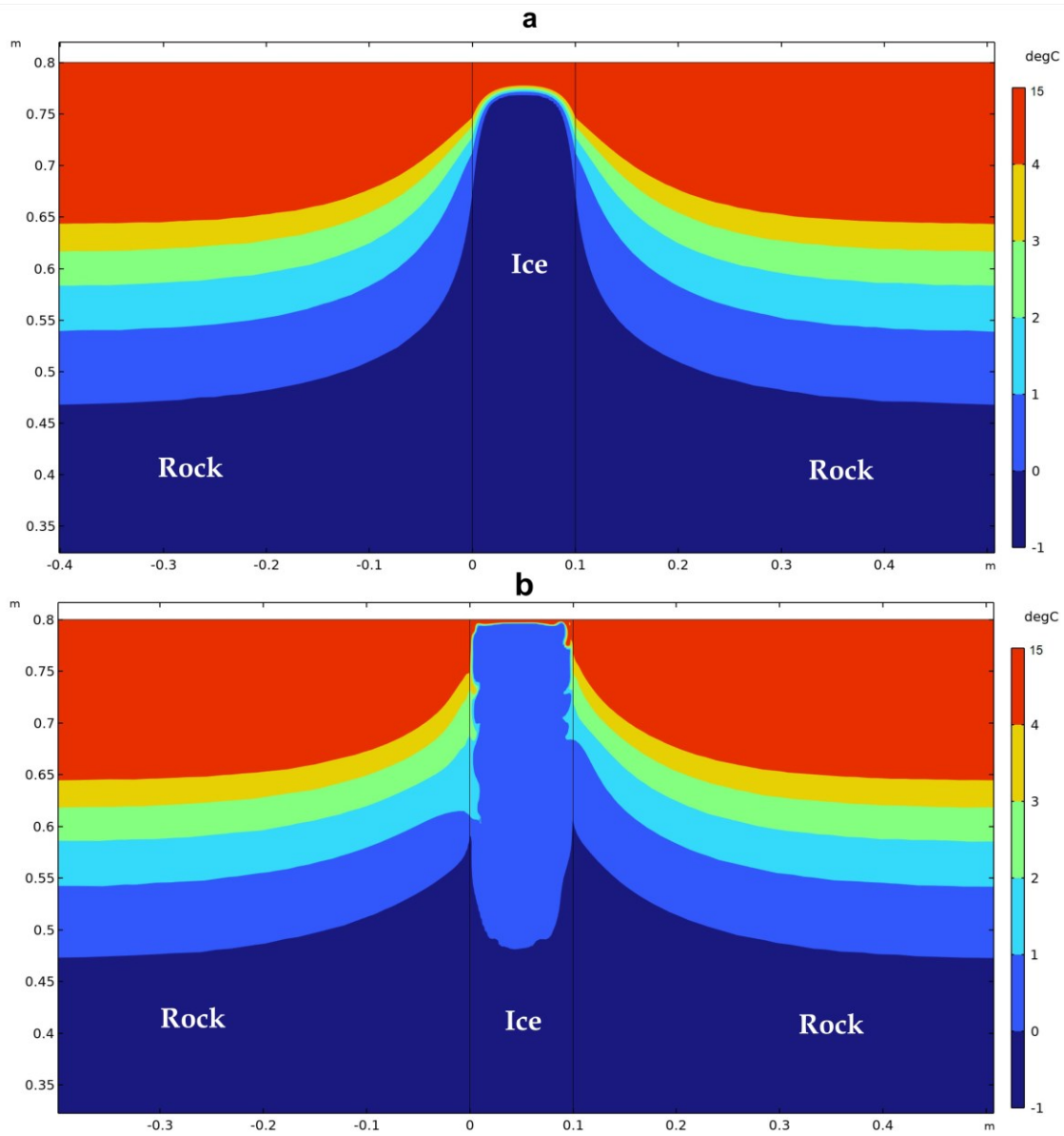
Figure 8. Temperature contour at t=9 hr for a) stagnant liquid water (SLW) and b) free convection (FC).
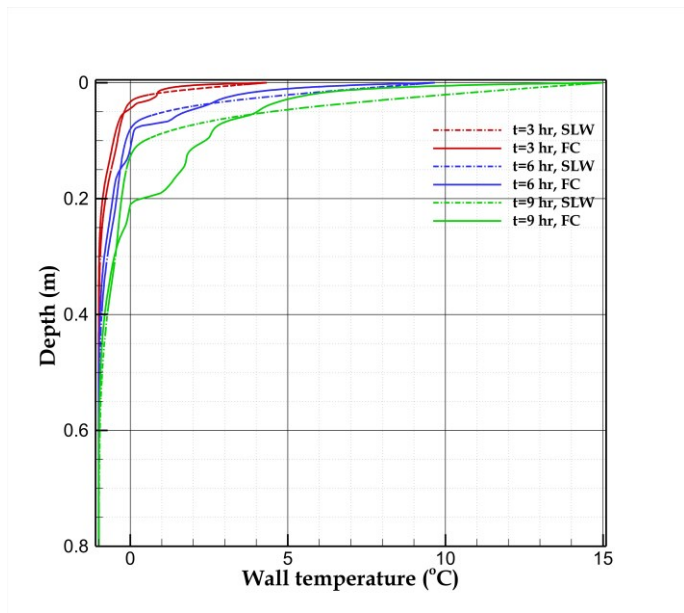
Figure 9. Left wall (rock-water interface) temperature as a function of depth) for stagnant liquid water (SLW) and free convection (FC).

245

Figure 10 displays the velocity magnitude as well as the flow in the water domain at different times. Vanishingly small velocity is predicted by the model wherever the water fraction is zero. Liquid water circulations generate a range of local velocities mixing the water and homogenizing the water temperature. As the melting of ice advances and the meltwater amount increases the velocity of water within the mixing zone increases, thereby accentuating the significance of free convective flux.

250
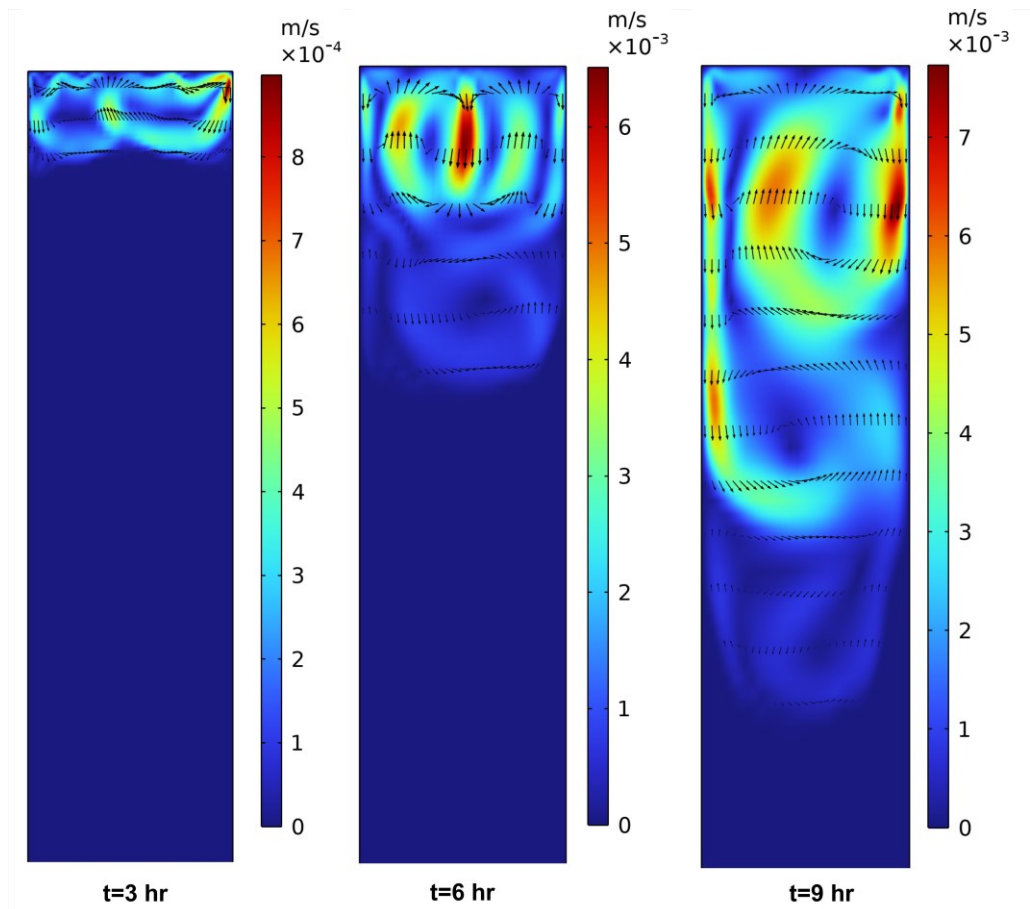
Figure 10. Velocity magnitude field in the upper 40 cm of the ice-cleft at different times. Zero velocity shows solid ice.

4.2 The effect of aperture size on melting rates

The cleft aperture determines the size of the domain and controls the initial ice mass. We considered the aperture sizes 2, 10, 20 and 50 cm in the parametric study. In order to remove the effect of cross-sectional area associated with different aperture sizes, we refer to the melting rate per unit of cross-sectional area (kg/hr/m^2).

Figure 11 illustrates the effect of the aperture size on the melting rate as a function of time. For the SLW case, heat transfer is mainly driven by diffusion in the rock, which has a greater diffusivity than water (see the temperature contour in Fig.8a). At a given depth, the rock is warmer than the water. The ice directly in contact with the rock thus melts faster. This explains the larger specific melting rate obtained with the smallest aperture (Ap=2 cm). In the presence of free convection, the melting rate after 9 hr is almost similar for the aperture sizes 2 and 10 cm (50 kg/hr/m^2). For greater aperture sizes, the effect of free

convection becomes more significant, resulting in the increase of the melting rate, which reaches about 110 kg/hr/m² for 50 cm aperture size. Figure 11 shows that the melting rate considering free convection with a 2 cm aperture-size (50 kg/hr/m²) is about twice the rate of the purely conduction case. For higher aperture sizes the difference in melting rates reaches about an order of magnitude.

265 In the present work, we simulated 9 hours of atmosphere temperature increase. When the aperture size A_p was varied from 2 to 50 cm, the liquid height H at the end of the simulation approximately ranged from 30 to 40 cm, and the convection cell occupied the entire liquid domain. However, the liquid height reached after 9 hours is only a small part of the actual height of the cleft (commonly up to 10 m). H is expected to increase if longer times are considered. The question arises whether the free convection cells always fill the entire liquid domain at longer times, despite the increase of friction due to lower aspect ratio

270 A_p/H. If the convection cell occupies only a part of the cavity, the efficiency of heat transfer between the ground surface and the melting front will be reduced. The significance of free convection can be assessed from the value of the dimensionless Rayleigh number

$$Ra = \frac{g\beta(T_c - T_H)H^3}{\alpha_l \, \nu_l} \tag{15}$$

where $(T_c\text{-}T_H)$ is the temperature difference between bottom and top surfaces, $\alpha_l = k_l/(\rho_l c_{pl})$ and $\nu_l = \mu_l/\rho_l$ are the liquid

275 water diffusivity and kinematic viscosity, respectively. Ra represents the ratio of the diffusion time over the free convection time ($Ra \sim 10^8$ in the numerical experiments presented in this article). In a cavity with infinite lateral dimensions (i.e., for $A_p/H \to \infty$), free convection is triggered for $Ra \gtrsim 10^3$ (otherwise, the conductive state is stable, see Bergman et al., (2017) for more information about the Rayleigh-Bénard instability). However, in the confined geometry considered in this work, the presence of the vertical walls must be considered. Rohsenow et al (1998) provide the following condition for convection onset,

280 which takes into account the stabilizing effect of the vertical walls for $A_p \ll H$, in the limiting case of perfectly conducting walls:

$$Ra \gtrsim 10^2 \times \left(\frac{H}{A_p}\right)^4 \tag{16}$$

Injecting Eq.(15) in Eq.(16) yields the maximum value of the liquid height H for which the free convection cell extends from the ground surface to the melting front:

$$H \lesssim 10^{-2} \times \frac{g\beta(T_c - T_H)A_p^4}{\alpha_l \, \nu_l} \tag{17}$$

Considering that the liquid region at temperature $T>4°C$ is stable and that the isotherm 4°C is close to the top of the cleft when

285 the free convection cell fills the entire cavity (see Fig. 8-b), we get $(T_c\text{-}T_H) =$-4°C. Using the physical properties from section 2.3 and $A_p = 2$ cm (the minimum aperture size considered in this study) yields $H \lesssim 10$ m, which is also the order of

magnitude of the maximum cleft height. Therefore, free convection cells should always extend throughout the melted region for $A_p \gtrsim 2$ cm. Note that the assumption of perfectly conducting walls used in Eq.(16) is less favorable to convection than finite conductivity (Rohsenow et al, 1998). Eq.(17) is thus expected to underestimate the higher bound of H corresponding to fully developed free convection cells.
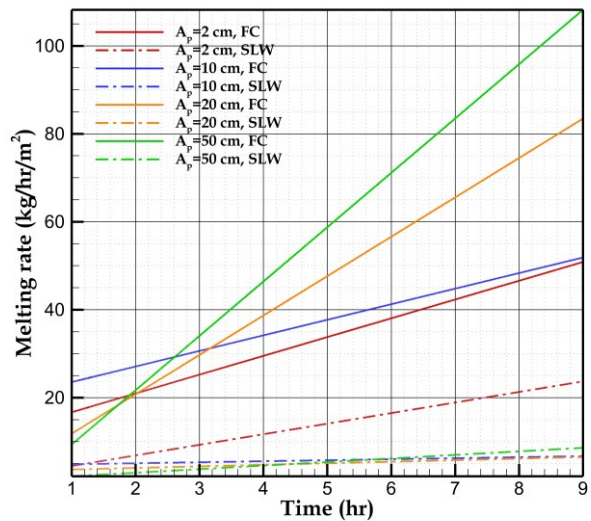
Figure 11. Effect of the aperture size on the melting rate for stagnant liquid water (SLW) and free convection (FC)

4.3 Application to field observations

The model is applied to a case-study from Monlesi ice cave, Switzerland (Luetscher et al., 2008). The main purpose is to qualitatively compare the field data with the model output and test how the pure conduction model can treat these problems. Monlesi ice cave is a low-elevation sporadic mountain permafrost site controlled by a peculiar ventilation regime associated with multiple cave entrances located at a similar elevation (Luetscher et al., 2008). The c. 600 m^2 cave chamber is partly filled with perennial congelation ice fed by a number of vertical clefts with width ranging from 10^1 to 10^3 mm. Seasonal freezing seals them periodically hindering any further water drainage from the epikarst (Fig. 12-a). The vertical distance between the external ground surface and the cave ceiling reaches c. 20 m. Seasonal and daily outside temperature fluctuations thaw the ice and freeze the meltwater in these rock clefts.

The main cleft (subcutaneous flow) was instrumented to measure discharge rates at 30 min intervals using a pressure probe set at the bottom of a 1 m long perforated PVC tube capturing the inlet. The water height measured in the tube is converted to

discharge (Q, in l/min) with an empirically calibrated rating curve checked by nine manual "bucket gauging" between 0 and

305   13 l/min with an uncertainty of ±10% (Luetscher et al., 2008).

Cave air temperatures were measured using negative temperature coefficient thermistors with a resistance of c.29.5 kOhm at 0°C and a temperature coefficient of about 5% °C-1 (YSI 44006). The thermistors were calibrated in a bath of melting ice to an accuracy of ±0.1°C. The thermistors were spaced at 2 m intervals in two chains comprising 19 sensors dispatched in the main cave chamber (Luetscher et al., 2008). Air temperatures were recorded at 1 h intervals and logged externally on a

310   Campbell CR10X data logger with two multiplexer logging units.

Figure 12-b displays the atmosphere and the soil temperature at 10 cm depth during 4.5 days (from April 13 to 17). No rainfall is recorded during this time period and the surface is free of snow. The soil temperature increases with a regular trend between 0 and 5 °C and is noticeably attenuated compared to atmosphere temperature fluctuations. The cave temperature is almost constant around -1 °C implying there is no melting from the bottom of the ice cleft. The atmosphere daily temperature variation

315   induces a water flow rate (0-12 l/min) with a trend similar to the surface temperature, supporting an origin associated with melting process of ice-filled clefts surrounding the cave.

To assess the melting rate, we considered the same conceptual model as in Fig. 1. A linear temperature rise from 0 to 5 °C during 4.5 days was assumed at the top boundary (black dash-dotted line in Fig. 12-b). This temperature rise is similar to the temperature evolution measured in the soil (solid black line in Fig.12b). In contrast to our model, meltwater drains deeper into

320   the subsurface. The uncertainty about the cleft geometry is, however, very high and we do not know how many fissures feed this water inlet. While our conceptual model is based on a closed cavity for the ease of simulation, the ice-filled cleft can be connected to a network of partially saturated smaller clefts (as in the epikarst) which drain the meltwater to the main vertical inlet at the top wall of Monlesi cave. Eventually, our simplified 2D geometry only approaches the real 3D-environment since other convection cells emerge along the cavity width which cannot be modeled in 2D.

325   A rough estimate of the cavity geometry (computational domain) assumes an initial ice-filled cleft with 3 meters depth (H_{dom}=3 m),10 cm aperture size (A_p=10 cm) and a typical length in the order of 1 m. The modelled melting rate is in the same order of magnitude as the water flow rate measured in the cave (red dash-dotted in Fig. 12-b). A purely conduction-based model underestimates the melting rate by >1 order of magnitude as compared to the case considering free convection (dashed in Fig. 12-b).

330
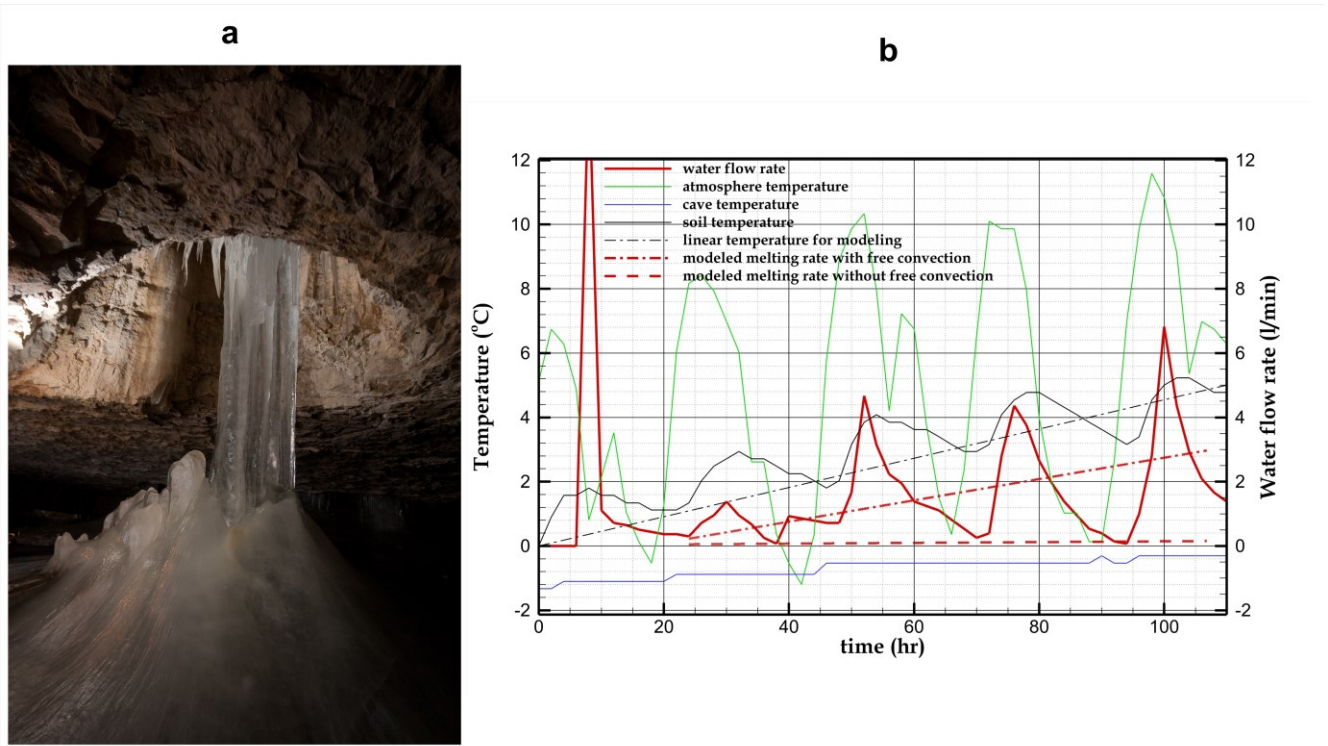
Figure 12. a) ice filled cleft in Monlesi cave b) field data including atmosphere (green), the soil (black) and cave temperature (blue) as well as the water flow rate measured at the fissure outlet (red) in Monlesi cave. The modelled melting rate considering free convection (red dashed dotted line) is compared to a case including only heat conduction (red dashed lines).

5 Discussion

In this study, we assumed a constant aperture size for modeling ice melt at daily time scale, but it should be noted that in the long-term, the repeated freeze-thaw cycles can deteriorate the hostrock clefts due to propagation and coalescence of older ones. Maji and Murton (Maji and Murton, 2021) investigated the mechanism and transition of microcracking and macrocracking

335   during freezing and thawing and developed a statistical modeling of crack propagation dynamics based on tension and shearing. Our results show that, under similar thermal configurations, conduction may not be the principal heat flux and permafrost degradation in heterogenous and ice-rich media may be much faster than anticipated. This is particularly relevant at high-elevation where a clear relationship is observed between rockfall activity and permafrost thawing (Gruber et al., 2004; Ravanel and Deline, 2011; Savi et al., 2021; Morino et al., 2021). In karst systems and fractured aquifers, where secondary porosity is

340   exceptionally well developed, frozen conduits/fractures may all of a sudden drain water into depth and change the local hydrological regime leading a thermal anomaly within the surrounding permafrost (Phillips et al., 2016). The subsequent freeze-thaw processes may lead to the precipitation of so-called cryogenic cave calcites (Žák et al., 2018), a secondary mineral precipitate increasingly used as proxy for paleo-permafrost conditions (Spötl et al., 2021; Töchterle et al., 2023). In contrast

to purely conductive systems, our results support a model where rapid hydrological recharge, e.g. due to extreme rainfall events, may accelerate the thawing of mountain permafrost (Luetscher et al., 2013) and thus questions classical interpretations for the formation of cryogenic calcites. But also at shallower depth, acknowledging the potential role of convective heat fluxes in ice-rich permafrost degradation may help predicting the rate of greenhouse gas releases, mainly carbon dioxide and methane, due to the decomposition of formerly frozen organic matter (Schaefer et al., 2014; Schuur et al., 2015). The intensity of free convection in soil depends strongly on the Rayleigh number which in turns depends on the permeability and dimensions of soil layer making it negligible, e.g. (Kane et al., 2001) or significant, e.g. (Jazi et al., 2024) with respect to the total heat transfer.

Pure water with a melting point at 0°C was considered in the present study. However, limestone dissolution results in the mineralization of the meltwater. Consequences are twofold: (1) the melting point is shifted to lower temperatures (in the range from -4 °C to 0 °C, see Tubini et al. (2021); McKenzie et al. (2007); Rühaak et al. (2015); (2) the variation of density with salt concentration could impact buoyancy, resulting in different flow patterns (thermosolutal convection, see for instance Mergui et al., 2002). The significance of the liquid phase composition could be assessed by numerical simulations, and should be considered in future works.

We did not consider any drainage of air or water inside the cleft or in its immediate vicinity. Forced convection induced by drainage could also contribute to the formation of a thermal bridge between the ground surface and the melting front, as suggested by Hasler et al., (2011). More work coupling field observations with numerical simulations including forced and free convection will be necessary to assess their relative significance, and determine the conditions under which one or the other effect dominates heat transfer.

6 Conclusion

A quantification of the melting rate of ice-rich permafrost in heterogeneous media is essential to assess the speed of permafrost degradation. Our model relies on a 2D approach coupling free convection (buoyancy-driven flow) in a vertical cleft with conduction in the surrounded homogeneous rock. Increasing the temperature of the ground surface can generate free convection cells because water-density increases between 0 and 4°C (a property specific to water). The convection cells generate a thermal bridge between the atmosphere and the melting front, resulting in the formation of a mixing zone with quasi-uniform temperature in the water column. This dramatically enhances the melting rate of interstitial ice when compared to models assuming stagnant liquid water (about an order of magnitude after 9 hours for an aperture size of 10 cm). In contrast to scenarios assuming conduction in stagnant liquid water, for which the temperature signal from the atmosphere is fully attenuated beyond a certain distance known as the diffusion length, the presence of free convection extends over greater distances. This thermal penetration also exerts an influence on the surrounding rock. Despite simplifying assumptions in the model and many uncertainties about the cleft geometry and the measured water flow rate, melting rate predicted by a model including free convection fit the order of magnitude measured in Monlesi cave (Fig. 12).

The significance of free convection should also be estimated in similar thermal configurations with different geometries such as cylindrical conduits or 3D cavities. Furthermore, the effect of free convection is not limited to hourly or daily oscillations and can be studied over much longer timescales, including centennial to millennial fluctuations. Currently, the computational costs are the main barriers for including free convection in long-term simulations. The full coupling of the momentum and

380 energy equations requires the time steps being much smaller compared to simple conduction-based models. Further investigations are thus ongoing to reformulate the governing equations and simplifying them for simulations over longer time-scales. Moreover, refreezing processes have yet to be considered to fully represent the long-term evolution of such a system. Eventually, the effect of water free convection on ice melting rate is not limited to permafrost regions. For instance, the melting of icebergs can also be impacted by water free convection (Couston et al., 2021; Hester et al., 2021) increasing production of

385 freshwater in oceans with potential impacts on the climate at global scale.

Appendix A: Sensitivity of the model to the melting temperature range ΔT.

The sensitivity of the melting rate to the melting temperature range ΔT is displayed in Fig.A1. Similar results are obtained for $\Delta T \leq \pm 0.7°C$. $\Delta T \leq \pm 0.5°C$ was thus selected in all simulations, as a value giving a good approximation of the pure water melting rate.

390
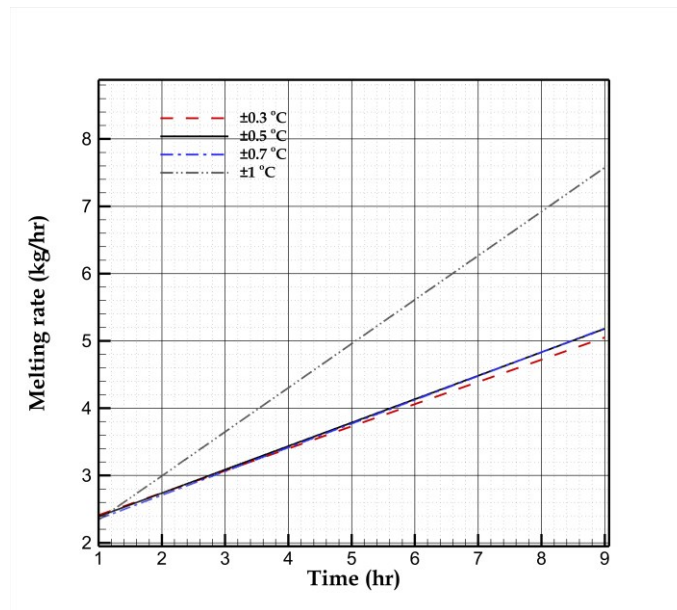
Figure A1. Effect of the melting temperature range ΔT on the melting rate predicted by the model (FC case, A_p=10 cm, H_{dom}=0.8 m, W_{dom}= 1 m .)

Software availability. The Comsol file (closed source software) is available upon request.

Video supplement. The animations of ice fraction evolution are available at https://doi.org/10.5281/zenodo.8435168.

Author contributions. AS completed the modelling work and wrote the original manuscript. ML designed the study together with AS and contributed with field data from Monlesi ice cave. All authors discussed the results and contributed to the final edition of the paper.

Competing interests. The authors declare that they have no competing interests.

Acknowledgements. This project is supported by the Swiss National Science Foundation (project n°200021_188636).

Reference

Andresen, C. G., Lawrence, D. M., Wilson, C. J., McGuire, A. D., Koven, C., Schaefer, K., Jafarov, E., Peng, S., Chen, X., and Gouttevin, I.: Soil moisture and hydrology projections of the permafrost region– a model intercomparison, Cryosph., 14, 445–459, 2020.

Arosemena, A.: Numerical Model of MeltingProblems, 2018.

Bartelt, P. and Lehning, M.: A physical SNOWPACK model for the Swiss avalanche warning: Part I: numerical model, Cold Reg. Sci. Technol., 35, 123–145, 2002.

Bartolomé, M., Cazenave, G., Luetscher, M., Spötl, C., Gázquez, F., Belmonte, Á., Turchyn, A. V., López-Moreno, J. I., and Moreno, A.: Mountain permafrost in the Central Pyrenees: insights from the Devaux ice cave, Cryosph., 17, 477–497, 2022.

Bejan, A.: Convection heat transfer, John wiley & sons, 2013.

Bense, V. F., Kooi, H., Ferguson, G., and Read, T.: Permafrost degradation as a control on hydrogeological regime shifts in a warming climate, J. Geophys. Res. Earth Surf., 117, 2012.

Bergman, T. L., Lavine, A. S., Incropera, F. P., and DeWitt, D. P.: Fundamentals of Heat and Mass Transfer, Wiley, 2017.

Bourdillon, A. C., Verdin, P. G., and Thompson, C. P.: Numerical simulations of water freezing processes in cavities and cylindrical enclosures, Appl. Therm. Eng., 75, 839–855, 2015.

Caggiano, A., Mankel, C., and Koenders, E.: Reviewing theoretical and numerical models for PCM-embedded cementitious composites, Buildings, 9, 3, 2018.

Cheng, G.: A roadbed cooling approach for the construction of Qinghai–Tibet Railway, Cold Reg. Sci. Technol., 42, 169–176, 2005.

Cicoira, A., Beutel, J., Faillettaz, J., Gärtner-Roer, I., and Vieli, A.: Resolving the influence of temperature forcing through heat conduction on rock glacier dynamics: a numerical modelling approach, Cryosph., 13, 927–942, 2019.

Colucci, R. R. and Guglielmin, M.: Climate change and rapid ice melt: Suggestions from abrupt permafrost degradation and ice melting in an alpine ice cave, Prog. Phys. Geogr. Earth Environ., 43, 561–573, 2019.

Comsol Multiphysics: v. 6.1 www. comsol. com COMSOL AB, Stockholm, Sweden.

Couston, L.-A., Hester, E., Favier, B., Taylor, J. R., Holland, P. R., and Jenkins, A.: Topography generation by melting and freezing in a turbulent shear flow, J. Fluid Mech., 911, A44, 2021.

Covington, M. D., Luhmann, A. J., Gabrovšek, F., Saar, M. O., and Wicks, C. M.: Mechanisms of heat exchange between water and rock in karst conduits, Water Resour. Res., 47, 2011.

Duvillard, P.-A., Ravanel, L., Schoeneich, P., Deline, P., Marcer, M., and Magnin, F.: Qualitative risk assessment and strategies for infrastructure on permafrost in the French Alps, Cold Reg. Sci. Technol., 189, 103311, 2021.

Fabre, C., Sauvage, S., Tananaev, N., Srinivasan, R., Teisserenc, R., and Sánchez Pérez, J. M.: Using modeling tools to better understand permafrost hydrology, Water, 9, 418, 2017.

Fohlmeister, J., Luetscher, M., Spötl, C., Schröder-Ritzrau, A., Schröder, B., Frank, N., Eichstädter, R., Trüssel, M., Skiba, V., and Boers, N.: The role of Northern Hemisphere summer insolation for millennial-scale climate variability during the penultimate glacial, Commun. Earth Environ., 4, 245, 2023.

Ford, D. and Williams, P. D.: Karst hydrogeology and geomorphology, John Wiley & Sons, 2007.

Fortier, R., LeBlanc, A.-M., and Yu, W.: Impacts of permafrost degradation on a road embankment at Umiujaq in Nunavik (Quebec), Canada, Can. Geotech. J., 48, 720–740, 2011.

Galushkin, Y.: Numerical simulation of permafrost evolution as a part of sedimentary basin modeling: permafrost in the Pliocene–Holocene climate history of the Urengoy field in the West Siberian basin, Can. J. Earth Sci., 34, 935–948, 1997.

Gruber, S., Hoelzle, M., and Haeberli, W.: Permafrost thaw and destabilization of Alpine rock walls in the hot summer of 2003, Geophys. Res. Lett., 31, 2004.

Guerrier, B., Doumenc, F., Roux, A., Mergui, S., and Jeannin, P.-Y.: Climatology in shallow caves with negligible ventilation: Heat and mass transfer, Int. J. Therm. Sci., 146, 106066, 2019.

Guyon, E., Hulin, J. P., Petit, L., and Mitescu, C. D.: Physical hydrodynamics, Oxford university press, 2015.

Haberkorn, A., Kenner, R., Noetzli, J., and Phillips, M.: Changes in ground temperature and dynamics in mountain permafrost in the Swiss Alps, Front. Earth Sci., 9, 626686, 2021.

Haeberli, W., Schaub, Y., and Huggel, C.: Increasing risks related to landslides from degrading permafrost into new lakes in de-glaciating mountain ranges, Geomorphology, 293, 405–417, 2017.

Hasler, A., Gruber, S., Font, M., and Dubois, A.: Advective heat transport in frozen rock clefts: Conceptual model, laboratory experiments and numerical simulation, Permafr. Periglac. Process., 22, 378–389, 2011.

Hayward, J. L., Jackson, A. J., Yost, C. K., Hansen, L. T., and Jamieson, R. C.: Fate of antibiotic resistance genes in two Arctic tundra wetlands impacted by municipal wastewater, Sci. Total Environ., 642, 1415–1428, 2018.

460   Heitz, W. L. and Westwater, J. W.: Extension of the numerical method for melting and freezing problems, Int. J. Heat Mass Transf., 13, 1371–1375, 1970.

Hester, E. W., McConnochie, C. D., Cenedese, C., Couston, L.-A., and Vasil, G.: Aspect ratio affects iceberg melting, Phys. Rev. Fluids, 6, 23802, 2021.

Hornum, M. T., Hodson, A. J., Jessen, S., Bense, V., and Senger, K.: Numerical modelling of permafrost spring discharge and

465   open-system pingo formation induced by basal permafrost aggradation, Cryosph., 14, 4627–4651, 2020.

Huss, M., Farinotti, D., Bauder, A., and Funk, M.: Modelling runoff from highly glacierized alpine drainage basins in a changing climate, Hydrol. Process., 22, 3888–3902, 2008.

Ivanov, V. and Rozhin, I.: Numerical simulation of the permafrost thawing near the city of Yakutsk during climate change up to the year 2100, in: AIP Conference Proceedings, 20050, 2022.

470   Jafarov, E. E., Marchenko, S. S., and Romanovsky, V. E.: Numerical modeling of permafrost dynamics in Alaska using a high spatial resolution dataset, Cryosph., 6, 613–624, 2012.

Jazi, F. N., Ghasemi-Fare, O., and Rockaway, T. D.: Natural convection effect on heat transfer in saturated soils under the influence of confined and unconfined subsurface flow, Appl. Therm. Eng., 237, 121805, 2024.

Jin, X.-Y., Jin, H.-J., Iwahana, G., Marchenko, S. S., Luo, D.-L., Li, X.-Y., and Liang, S.-H.: Impacts of climate-induced

475   permafrost degradation on vegetation: A review, Adv. Clim. Chang. Res., 12, 29–47, 2021.

Kahraman, R., Zughbi, H. D., and Al-Nassar, Y. N.: A numerical simulation of melting of ice heated from above, Math. Comput. Appl., 3, 127–137, 1998.

Kane, D. L., Hinkel, K. M., Goering, D. J., Hinzman, L. D., and Outcalt, S. I.: Non-conductive heat transfer associated with frozen soils, Glob. Planet. Change, 29, 275–292, 2001.

480   Krumhansl, K. A., Krkosek, W. H., Greenwood, M., Ragush, C., Schmidt, J., Grant, J., Barrell, J., Lu, L., Lam, B., and Gagnon, G. A.: Assessment of Arctic community wastewater impacts on marine benthic invertebrates., Environ. Sci. Technol., 49, 760–766, 2015.

Larsen, P. H., Goldsmith, S., Smith, O., Wilson, M. L., Strzepek, K., Chinowsky, P., and Saylor, B.: Estimating future costs for Alaska public infrastructure at risk from climate change, Glob. Environ. Chang., 18, 442–457, 2008.

485   Luetscher, M., Lismonde, B., and Jeannin, P.: Heat exchanges in the heterothermic zone of a karst system: Monlesi cave, Swiss Jura Mountains, J. Geophys. Res. Earth Surf., 113, 2008.

Luetscher, M., Borreguero, M., Moseley, G. E., Spötl, C., and Edwards, R. L.: Alpine permafrost thawing during the Medieval Warm Period identified from cryogenic cave carbonates, Cryosph., 7, 1073–1081, 2013.

Luetscher, M., Boch, R., Sodemann, H., Spötl, C., Cheng, H., Edwards, R. L., Frisia, S., Hof, F., and Müller, W.: North Atlantic

490   storm track changes during the Last Glacial Maximum recorded by Alpine speleothems, Nat. Commun., 6, 6344, 2015.

Maji, V. and Murton, J. B.: Experimental observations and statistical modeling of crack propagation dynamics in limestone by acoustic emission analysis during freezing and thawing, J. Geophys. Res. Earth Surf., 126, e2021JF006127, 2021.

Malakhova, V. V: Numerical modeling of methane hydrates dissociation in the submarine permafrost, in: IOP Conference Series: Earth and Environmental Science, 12022, 2022.

495   Marchenko, S., Romanovsky, V., and Tipenko, G.: Numerical modeling of spatial permafrost dynamics in Alaska, in: Proceedings of the ninth international conference on permafrost, 1125–1130, 2008.

McKenzie, J. M., Voss, C. I., and Siegel, D. I.: Groundwater flow with energy transport and water–ice phase change: numerical simulations, benchmarks, and application to freezing in peat bogs, Adv. Water Resour., 30, 966–983, 2007.

Mergui, S., Geoffroy, S., and Be´nard, C.: Ice block melting into a binary solution: Coupling of the interfacial equilibrium
500   and the flow structures, J. Heat Transf., 124, 1147–1157, 2002.

Michałek, T. and Kowalewski, T. A.: Simulations of the water freezing process–numerical benchmarks, Task Q., 7, 389–408, 2003.

Mohammed, A. A., Bense, V. F., Kurylyk, B. L., Jamieson, R. C., Johnston, L. H., and Jackson, A. J.: Modeling reactive solute transport in permafrost-affected groundwater systems, Water Resour. Res., 57, e2020WR028771, 2021.

505   Morino, C., Conway, S. J., Balme, M. R., Helgason, J. K., Sæmundsson, Þ., Jordan, C., Hillier, J., and Argles, T.: The impact of ground-ice thaw on landslide geomorphology and dynamics: two case studies in northern Iceland, Landslides, 18, 2785–2812, 2021.

Mousavi Ajarostaghi, S. S., Poncet, S., Sedighi, K., and Aghajani Delavar, M.: Numerical modeling of the melting process in a shell and coil tube ice storage system for air-conditioning application, Appl. Sci., 9, 2726, 2019.

510   Nazzi Ehms, J. H., De Césaro Oliveski, R., Oliveira Rocha, L. A., Biserni, C., and Garai, M.: Fixed grid numerical models for solidification and melting of phase change materials (PCMs), Appl. Sci., 9, 4334, 2019.

Noetzli, J., Arenson, L. U., Bast, A., Beutel, J., Delaloye, R., Farinotti, D., Gruber, S., Gubler, H., Haeberli, W., and Hasler, A.: Best practice for measuring permafrost temperature in boreholes based on the experience in the Swiss Alps, Front. Earth Sci., 9, 607875, 2021.

515   Painter, S. L., Coon, E. T., Atchley, A. L., Berndt, M., Garimella, R., Moulton, J. D., Svyatskiy, D., and Wilson, C. J.: Integrated surface/subsurface permafrost thermal hydrology: Model formulation and proof-of-concept simulations, Water Resour. Res., 52, 6062–6077, 2016.

Pelletier, M., Allard, M., and Levesque, E.: Ecosystem changes across a gradient of permafrost degradation in subarctic Québec (Tasiapik Valley, Nunavik, Canada), Arct. Sci., 5, 1–26, 2018.

520   Pham, H.-N., Arenson, L. U., and Sego, D. C.: Numerical analysis of forced and natural convection in waste-rock piles in permafrost environments, in: Proceedings of the Ninth International Conference on Permafrost, 2008.

Phillips, M., Haberkorn, A., Draebing, D., Krautblatter, M., Rhyner, H., and Kenner, R.: Seasonally intermittent water flow through deep fractures in an Alpine Rock Ridge: Gemsstock, Central Swiss Alps, Cold Reg. Sci. Technol., 125, 117–127,

2016.

525 Pruessner, L., Huss, M., Phillips, M., and Farinotti, D.: A framework for modeling rock glaciers and permafrost at the basin-scale in high alpine catchments, J. Adv. Model. Earth Syst., 13, e2020MS002361, 2021.

Ravanel, L. and Deline, P.: Climate influence on rockfalls in high-Alpine steep rockwalls: The north side of the Aiguilles de Chamonix (Mont Blanc massif) since the end of the 'Little Ice Age,' The Holocene, 21, 357–365, 2011.

Rohsenow, W. M., Hartnett, J. P., and Cho, Y. I.: Handbook of heat transfer, Mcgraw-hill New York, 1998.

530 Rühaak, W., Anbergen, H., Grenier, C., McKenzie, J., Kurylyk, B. L., Molson, J., Roux, N., and Sass, I.: Benchmarking numerical freeze/thaw models, Energy Procedia, 76, 301–310, 2015.

Savi, S., Comiti, F., and Strecker, M. R.: Pronounced increase in slope instability linked to global warming: A case study from the eastern European Alps, Earth Surf. Process. Landforms, 46, 1328–1347, 2021.

Schaefer, K., Lantuit, H., Romanovsky, V. E., Schuur, E. A. G., and Witt, R.: The impact of the permafrost carbon feedback

535 on global climate, Environ. Res. Lett., 9, 85003, 2014.

Schuster, P. F., Schaefer, K. M., Aiken, G. R., Antweiler, R. C., Dewild, J. F., Gryziec, J. D., Gusmeroli, A., Hugelius, G., Jafarov, E., and Krabbenhoft, D. P.: Permafrost stores a globally significant amount of mercury, Geophys. Res. Lett., 45, 1463–1471, 2018.

Schuur, E. A. G., McGuire, A. D., Schädel, C., Grosse, G., Harden, J. W., Hayes, D. J., Hugelius, G., Koven, C. D., Kuhry,

540 P., and Lawrence, D. M.: Climate change and the permafrost carbon feedback, Nature, 520, 171–179, 2015.

Sedaghatkish, A. and Luetscher, M.: Modeling the effect of free convection on permafrost melting-rates in frozen rock-clefts, , https://doi.org/10.5281/zenodo.8435168, n.d.

Spiegel, E. A. and Veronis, G.: On the Boussinesq approximation for a compressible fluid., Astrophys. Journal, vol. 131, p. 442, 131, 442, 1960.

545 Spötl, C., Koltai, G., Jarosch, A. H., and Cheng, H.: Increased autumn and winter precipitation during the Last Glacial Maximum in the European Alps, Nat. Commun., 12, 1839, 2021.

Töchterle, P., Baldo, A., Murton, J. B., Schenk, F., Edwards, R. L., Koltai, G., and Moseley, G. E.: Reconstructing Younger Dryas Ground Temperature and Snow Thickness from Cave Deposits, Clim. Past Discuss., 2023, 1–21, 2023.

Tubini, N., Gruber, S., and Rigon, R.: A method for solving heat transfer with phase change in ice or soil that allows for large

550 time steps while guaranteeing energy conservation, Cryosph., 15, 2541–2568, 2021.

Virag, Z., Živić, M., and Galović, A.: Influence of natural convection on the melting of ice block surrounded by water on all sides, Int. J. Heat Mass Transf., 49, 4106–4115, 2006.

Walvoord, M. A. and Kurylyk, B. L.: Hydrologic impacts of thawing permafrost—A review, Vadose Zo. J., 15, 2016.

Weast, R. C.: CRC handbook of chemistry and physics., 1986.

555 Wind, M., Obleitner, F., Racine, T., and Spötl, C.: Multi-annual temperature evolution and implications for cave ice development in a sag-type ice cave in the Austrian Alps, Cryosph., 16, 3163–3179, 2022.

Žák, K., Onac, B. P., Kadebskaya, O. I., Filippi, M., Dublyansky, Y., and Luetscher, M.: Cryogenic mineral formation in

caves, in: Ice caves, Elsevier, 123–162, 2018.

Zeneli, M., Malgarinos, I., Nikolopoulos, A., Nikolopoulos, N., Grammelis, P., Karellas, S., and Kakaras, E.: Numerical
560   simulation of a silicon-based latent heat thermal energy storage system operating at ultra-high temperatures, Appl. Energy,
242, 837–853, 2019.

Zhang, M., Lai, Y., Liu, Z., and Gao, Z.: Nonlinear analysis for the cooling effect of Qinghai-Tibetan railway embankment
with different structures in permafrost regions, Cold Reg. Sci. Technol., 42, 237–249, 2005.

565